The 2010 IEEE/RSJ International Conference on
Intelligent Robots and Systems
October 18-22, 2010, Taipei, Taiwan

Optimization of Impact Motions for Humanoid Robots Considering Multibody Dynamics and Stability

Teppei Tsujita, Atsushi Konno and Masaru Uchiyama

Abstract— **In order to exert large force on an environment, it is effective to apply impulsive force. We describe the motions that perform tasks by applying impulsive force as "impact motion." The objective of an impact motion is to exert large force on an environment, however if the impulsive force is too large, the robot may fall down due to the reaction force. This paper presents an optimization scheme to generate impact motions for humanoid robots. The advantage of the proposed scheme is that impulsive force exerted on a target by a humanoid robot's whole body is maximized while guaranteeing the stability. A punching motion is generated by the scheme as an example and evaluated by performing simulations.**

I. INTRODUCTION

When a robot applies force statically on an environment, the magnitude of the force is limited by the maximum torque of its actuators. In order to exert large force on the environment beyond this limitation, it is effective to apply impulsive force. For example, if a robot pushes a nail statically by a hammer, the nail cannot be inserted into a wood. However, the nail can be driven by hitting by the hammer since momentum of a hammer and a robot is exerted in a short time. We describe the motions that perform tasks by applying impulsive force as "impact motion." There are difficult problems introduced by impacts between robots and environments.

Uchiyama proposed a control algorithm constitution method and dynamic control modes for performing a nailing task by a 3 DOF manipulator [1]. Asada and Ogawa proposed the *virtual mass* for analyzing dynamic behavior of a manipulator arm and its end effector that interacts with the environment [2]. Around the same time, Khatib and Burdick proposed the *effective mass* [3]. These works mentioned above used robotic manipulators fixed on the ground.

When a humanoid robot exerts impulsive force on a target object, reaction force may bring the humanoid robot down. A few attempts on tasks applying impulsive force by a humanoid robot have been reported in recent years. Konno et al. proposed an optimization scheme of impact motions for humanoid robot [4]. In this research, impact motions are optimized based on the *virtual mass*. However, this scheme did not consider stability at the time of impact. Arisumi and Yokoi investigated a method to push a door utilizing impulsive force by a humanoid robot [5]. In this research, the humanoid robot is treated as a rigid single body. However, when a humanoid robot exerts a impulsive force by its end effector, the effect of the servo stiffness cannot be ignored. This paper presents optimization scheme of impact motions considering multibody dynamics and stability for humanoid robots. By using a dynamics computation method [6], the force exerted on a target by a humanoid robot's whole body is maximized while guaranteeing the stability. In order to avoid falling during the impact motion, relationship between ZMP(Zero-Moment Point) [7] and a support polygon is evaluated in all phase in the optimization process.

This research was supported by NEDO Industrial Technology Research Grant Program (project ID: 05A30703a) and JSPS Grant-in-Aid for JSPS Fellows (20·6273).

T. Tsujita, A. Konno and M. Uchiyama are with Department of Aerospace Engineering, Tohoku University, Aoba-yama 6-6-01, Japan. tsujita@space.mech.tohoku.ac.jp

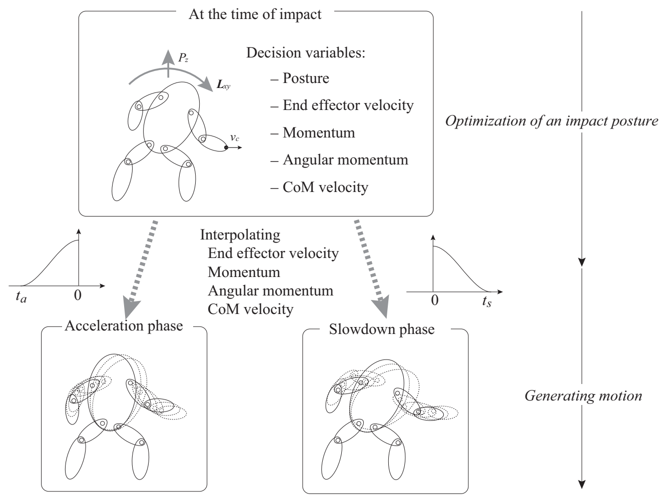

Fig. 1. Outline of the motion generation scheme.

II. OUTLINE OF MOTION GENERATION SCHEME

An impact motion is divided into three phases as follows in this paper.

Acceleration phase: A robot accelerates its joints to hit a target object during this phase.

Impact phase: During this phase, the robot hits the target. This phase is short time just before and after contact.

Slowdown phase: The robot decelerates its joints after hitting the target and stands still during this phase.

Fig. 1 shows an outline of the proposed motion generating method. This method consists of two parts.

i) Optimizing an impact posture and joint velocities at the time of impact.
ii) Generating motions for acceleration and slowdown phases.

In the first stage, the posture and joint velocities are decided under constraints to maximize the impulsive force or impulse exerted on a target. By using the simplified dynamics computation (SDC) model [6], the impulsive force and impulse can be estimated. Moreover, behavior of ZMP during the impact phase can be obtained. However, it is not known how stable the robot is during the acceleration and slowdown phases at this stage. Hence, there is a possibility of generating motion which is unstable during the acceleration and slowdown phase even if the impact posture and velocities are stable during the impact phase. Therefore, the following steps are considered to overcome the problem.

1) Setting decision variables(posture, end effector's velocity, momentum, angular momentum and velocity of CoM(Center of Mass)) at the time of impact and estimating impulsive force and ZMP during impact phase by the SDC model.
2) Interpolating the decision variables from zero and to zero and computing ZMP during acceleration and slowdown phases.
3) If the impulsive force is maximum under constraints, e.g., stability, the motion generation process proceeds to Step 4). If the force is not maximum, the decision variables are slightly changed and motion generation process returns to Step 1).
4) Generating motions for acceleration/slowdown phases to satisfy the interpolated trajectories in Step 2).

Since Step 1) and 2) are executed in optimization process, these steps are computed numerous times. The advantage of this scheme is that ZMP trajectory during acceleration/slowdown phases can be estimated in process 2) without computing the inverse dynamics.

ZMP can be expressed in the form.

$$P_{ZMPx} = \frac{MgP_{Gx} - \dot{L}_y}{Mg + \dot{P}_z}, \quad P_{ZMPy} = \frac{MgP_{Gy} + \dot{L}_x}{Mg + \dot{P}_z}, \quad (1)$$

where P_{ZMPx}, P_{ZMPy}, P_{Gx} and P_{Gy} are position of ZMP in X_b and Y_b directions and GCoM(Ground projection of Center of Mass) in X_b and Y_b directions, respectively. $\dot{L}_x$, $\dot{L}_y$ and $\dot{P}_z$ are differentiations of angular momentums around X_b and Y_b axes and momentum in Z_b direction, respectively. M and g are respectively total mass of the system and acceleration of gravity. This formula indicates that a time series ZMP trajectory can be computed using the CoM, angular momentum and momentum trajectories. Hence, by interpolating these values, ZMP trajectory can be obtained with low computation cost. Therefore, stability during the acceleration and slowdown phase can be evaluated in the optimizing process. By considering stability based on ZMP and a support polygon as a constraint condition, the optimizing problem outputs a stable motion in all phases.

III. IMPACT MOTION OPTIMIZATION

In this section, detail of the proposed impact motion optimization scheme is presented. Notations of the decision variables in Step 1) are denoted in Subsection III-A and III-B and a motion generation scheme in Step 4) is presented in Subsection III-C. Formulation of the optimization problem in Step 1) $\sim$ 3) is presented in Subsection III-D. Superscripts rl, ll, ra and la express the robot's right leg, left leg, right arm and left arm numbers, respectively and the total degree of freedom of the robot is n.

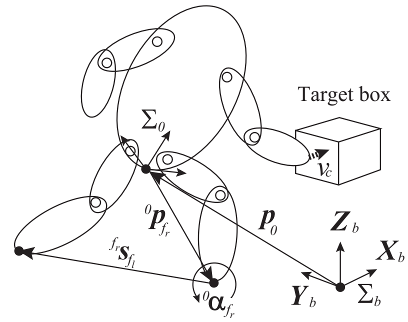

Fig. 2. A robot punches a target box.

A. Posture (Joint Angles)

Let's consider a situation when the humanoid robot hits a free floating target box in X_b direction as shown in Fig. 2. In the figure, Σ_b is the world coordinate system, Σ_0 is the robot body coordinate system, $^0\boldsymbol{p}_{f_r}$ is the position vector of the right foot with respect to Σ_0, $^{f_r}\boldsymbol{s}_{f_l}$ is the position vector of the left foot with respect to the right foot coordinate system and $^0\boldsymbol{\alpha}_{f_r}$ is the Z-Y-X Euler angle vector of the right foot with respect to Σ_0. Left superscripts 0 and f_r denote Σ_0 and the right foot coordinate system, respectively. Elements of $^0\boldsymbol{p}_{f_r}$, $^{f_r}\boldsymbol{s}_{f_l}$ and $^0\boldsymbol{\alpha}_{f_r}$ are denoted as follows.

$$\begin{aligned} {}^0\boldsymbol{p}_{f_r} &\equiv \begin{bmatrix} {}^0p_{x,f_r} & {}^0p_{y,f_r} & {}^0p_{y,f_r} \end{bmatrix}^T, \\ {}^{f_r}\boldsymbol{s}_{f_l} &\equiv \begin{bmatrix} {}^{f_r}s_{x,f_l} & {}^{f_r}s_{y,f_l} & {}^{f_r}s_{z,f_l} \end{bmatrix}^T, \\ {}^0\boldsymbol{\alpha}_{f_r} &\equiv \begin{bmatrix} {}^0\alpha_{x,f_r} & {}^0\alpha_{y,f_r} & {}^0\alpha_{z,f_r} \end{bmatrix}^T, \end{aligned}$$

where $^0p_{x,f_r}$ is the position of the right foot in X_b direction with respect to Σ_0 and the others are defined similarly.

The position and orientation of Σ_0 with respect to Σ_b is expressed as follows on the assumption that the right foot is fixed on the ground.

$$\boldsymbol{p}_0 = -\left({}^0\boldsymbol{R}_{f_r}\right)^T {}^0\boldsymbol{p}_{f_r}, \quad \boldsymbol{R}_0 = \left({}^0\boldsymbol{R}_{f_r}\right)^T \quad (2)$$

where $\boldsymbol{p}_0$ and $\boldsymbol{R}_0$ are the position vector and the rotation matrix of Σ_0 with respect to Σ_b. $^0\boldsymbol{R}_{f_r}$ expresses orientation of the right foot with respect to Σ_0. In this paper, position vectors and rotation matrices which does not have a left superscript are expressed with respect to Σ_b.

By this operation, the origin of the right foot is same with the origin of Σ_b. The joint angles of the right leg $\boldsymbol{\phi}^{rl} = \begin{bmatrix} \phi_1^{rl}, & \cdots & ,\phi_i^{rl}, & \cdots & ,\phi_{n_{rl}}^{rl} \end{bmatrix}^T$ can be obtained by inverse kinematics using $^0\boldsymbol{p}_{f_r}$ and $^0\boldsymbol{\alpha}_{f_r}$. The subscript i express the joint number which is numbered from a root link to a tip link and n_{rl} expresses maximum number of the right leg joints. The position of the left foot $^0\boldsymbol{p}_{f_r}$ can be calculated in the form:

$${}^0\boldsymbol{p}_{f_l} = {}^0\boldsymbol{p}_{f_r} + {}^0\boldsymbol{R}_{f_r}\, {}^{f_r}\boldsymbol{s}_{f_l}. \quad (3)$$

The joint angles of the left leg $\boldsymbol{\phi}^{ll} = \begin{bmatrix} \phi_1^{ll}, & \cdots & ,\phi_{n_{ll}}^{ll} \end{bmatrix}^T$ can be obtained on the assumption that the orientation of the left foot is the same with the right foot. n_{ll} expresses maximum number of the left leg joints. Therefore, the both legs' postures are defined by ${}^0\boldsymbol{p}_{f_r}$, ${}^0\boldsymbol{\alpha}_{f_r}$ and ${}^{fr}\boldsymbol{s}_{fl}$ under the kinematic closure constraint. In addition, by defining the joint angles except for the leg joints, the posture can be defined at the impact. The remaining joint angle vector is expressed as $\boldsymbol{\phi}^{rem}$.

B. Joint Velocities

The joint angle velocities are computed from the following values.

- Velocity of the end effector
- Momentum and angular momentum
- Velocity of the center of mass

The relationship between the joint angle velocities and the above mentioned values are expressed in the form:

$$\begin{bmatrix} \boldsymbol{v}_c \\ \boldsymbol{\omega}_c \\ \boldsymbol{P} \\ \boldsymbol{L} \\ \boldsymbol{v}_g \end{bmatrix} = \begin{bmatrix} \boldsymbol{J}_c(\boldsymbol{\phi}) \\ \boldsymbol{J}_{PL}(\boldsymbol{\phi}) \\ \boldsymbol{J}_{Tg}(\boldsymbol{\phi}) \end{bmatrix} \dot{\boldsymbol{\phi}}, \tag{4}$$

where

$$\dot{\boldsymbol{\phi}} \equiv \begin{bmatrix} \boldsymbol{\phi}^{rl} \\ \boldsymbol{\phi}^{ll} \\ \boldsymbol{\phi}^{rem} \end{bmatrix}, \ \boldsymbol{J}_{PL} \equiv \begin{bmatrix} \boldsymbol{J}_{P_x} \\ \boldsymbol{J}_{P_y} \\ \boldsymbol{J}_{P_z} \\ \boldsymbol{J}_{L_x} \\ \boldsymbol{J}_{L_y} \\ \boldsymbol{J}_{L_z} \end{bmatrix}, \ \boldsymbol{J}_{Tg} \equiv \begin{bmatrix} \boldsymbol{J}_{Tg_x} \\ \boldsymbol{J}_{Tg_y} \\ \boldsymbol{J}_{Tg_z} \end{bmatrix},$$

$\dot{\boldsymbol{\phi}} \in R^{n\times 1}$: joint velocity vector,
$\boldsymbol{v}_c \in R^{3\times 1}$: velocity of the collision point,
$\boldsymbol{\omega}_c \in R^{3\times 1}$: angular velocity of the collision point,
$\boldsymbol{P} \in R^{3\times 1}$: momentum of the whole system in Σ_b, $\boldsymbol{P} = \begin{bmatrix} P_x & P_y & P_z \end{bmatrix}^T$,
$\boldsymbol{L} \in R^{3\times 1}$: angular momentum of the whole system in Σ_b, $\boldsymbol{L} = \begin{bmatrix} L_x & L_y & L_z \end{bmatrix}^T$,
$\boldsymbol{v}_g \in R^{3\times 1}$: velocity vector of the center of mass, $\boldsymbol{v}_g = \begin{bmatrix} v_{gx} & v_{gy} & v_{gz} \end{bmatrix}^T$
$\boldsymbol{J}_c(\boldsymbol{\phi}) \in R^{6\times n}$: relational expression of $\dot{\boldsymbol{\phi}}$ and $\begin{bmatrix} \boldsymbol{v}_c & \boldsymbol{\omega}_c \end{bmatrix}^T$,
$\boldsymbol{J}_{PL}(\boldsymbol{\phi}) \in R^{6\times n}$: relational expression of $\dot{\boldsymbol{\phi}}$ and $\begin{bmatrix} \boldsymbol{P}^T & \boldsymbol{L}^T \end{bmatrix}^T$,
$\boldsymbol{J}_{Tg}(\boldsymbol{\phi}) \in R^{3\times n}$: relational expression of $\dot{\boldsymbol{\phi}}$ and $\boldsymbol{v}_g$.

$\boldsymbol{J}_{PL}(\boldsymbol{\phi})$ and $\boldsymbol{J}_{Tg}(\boldsymbol{\phi})$ for a multibody system are presented in [8]. In order to hit the target box as shown in Fig. 2, the end effector has collision velocity v_c in X_b direction. It is assumed that a humanoid robot illustrated in Fig. 2 moves its hand along X_b axis and hits a free floating target box with velocity v_c. Therefore, the velocity and angular velocity of the end effector in Σ_b are expressed as follows:

$$\begin{bmatrix} \boldsymbol{v}_c \\ \boldsymbol{\omega}_c \end{bmatrix} = \begin{bmatrix} v_c \boldsymbol{n}_x \\ \boldsymbol{0} \end{bmatrix}, \tag{5}$$

where $\boldsymbol{n}_x$ is an unit vector of X_b direction.

The velocity of CoM is dependent to the momentum of the whole system. The velocity can be obtained by dividing the momentum by the total mass. Therefore, the rows of $\boldsymbol{P}$ and $\boldsymbol{v}_g$ are not independent. From (1), only the velocity of GCoM, momentum in Z_b direction and angular momentum around X_b and Y_b affect the ZMP. Therefore, the dimensions of (4) can be reduced as follows:

$$\begin{bmatrix} \boldsymbol{v}_c \\ \boldsymbol{\omega}_c \\ P_z \\ L_x \\ L_y \\ v_{gx} \\ v_{gy} \end{bmatrix} = \begin{bmatrix} \boldsymbol{J}_c \\ \boldsymbol{J}_{P_z} \\ \boldsymbol{J}_{L_x} \\ \boldsymbol{J}_{L_y} \\ \boldsymbol{J}_{Tg_x} \\ \boldsymbol{J}_{Tg_y} \end{bmatrix} \dot{\boldsymbol{\phi}} \equiv \boldsymbol{J}_{hu}\dot{\boldsymbol{\phi}}, \tag{6}$$

In addition, the constraint conditions must be considered when there are kinematic closures.

$$\begin{bmatrix} \boldsymbol{V} \\ \boldsymbol{0} \end{bmatrix} = \begin{bmatrix} \boldsymbol{J}_{hu} \\ \boldsymbol{C}_\alpha \end{bmatrix} \dot{\boldsymbol{\phi}}, \tag{7}$$

where

$$\boldsymbol{V} \equiv \begin{bmatrix} \boldsymbol{v}_c \\ \boldsymbol{\omega}_c \\ \boldsymbol{\mathcal{M}} \\ \boldsymbol{v}_{Tg_{xy}} \end{bmatrix}, \quad \boldsymbol{\mathcal{M}} \equiv \begin{bmatrix} P_z \\ L_x \\ L_y \end{bmatrix}, \quad \boldsymbol{v}_{Tg_{xy}} \equiv \begin{bmatrix} v_{gx} \\ v_{gy} \end{bmatrix},$$

and $\boldsymbol{C}_\alpha \in R^{\alpha\times n}$ is the constraint formula and the size of column depends on the situation. For example, the kinematics closure of the legs is expressed by this constraint formula as follows to avoid generating internal forces in the situation where a humanoid robot stands with its both feet as shown in Fig. 2. In this case, the relative velocities which are generated by the both legs must be zero. Therefore, this constraint condition can be formulated in the form:

$$\boldsymbol{0} = \begin{bmatrix} \boldsymbol{J}_0 & -\boldsymbol{J}_0^{'} & \boldsymbol{0}, \cdots, \boldsymbol{0} \end{bmatrix} \dot{\boldsymbol{\phi}} \equiv \boldsymbol{C}_\alpha \dot{\boldsymbol{\phi}}, \tag{8}$$

where $\boldsymbol{J}_0$ expresses relationship between the velocities of Σ_0 generated by the right leg and the right leg joints and $\boldsymbol{J}_0^{'}$ expresses relationship between the velocities of Σ_0 generated by left leg and the left leg joints.

$$\boldsymbol{J}_0 \equiv \begin{bmatrix} -\boldsymbol{E} & {}^0\tilde{\boldsymbol{p}}_{f_r}^{\ T} \\ \boldsymbol{0} & -\boldsymbol{E} \end{bmatrix} {}^0\boldsymbol{J}_{f_r}, \ \boldsymbol{J}_0^{'} \equiv \begin{bmatrix} -\boldsymbol{E} & {}^0\tilde{\boldsymbol{p}}_{f_l}^{\ T} \\ \boldsymbol{0} & -\boldsymbol{E} \end{bmatrix} {}^0\boldsymbol{J}_{f_l},$$

where ${}^0\boldsymbol{J}_{f_r}$ express relationship between the joints and the velocities of the right foot with respect to Σ_0 and ${}^0\boldsymbol{J}_{f_l}$ express relationship between the joints and the velocities of the left foot with respect to Σ_0. And $\boldsymbol{E} \in R^{3\times 3}$ denotes an identity matrix. $\tilde{\boldsymbol{p}}$ is the skew-symmetric matrix to rewrite the cross product by matrix multiplication as $\tilde{\boldsymbol{p}}\boldsymbol{b} = \boldsymbol{p} \times \boldsymbol{b}$ where $\boldsymbol{b}$ is an arbitrary vector.

The simultaneous equation (7) describes the relationships between the joint angle velocities and the end effector velocities, the CoM velocity and the momentums under the

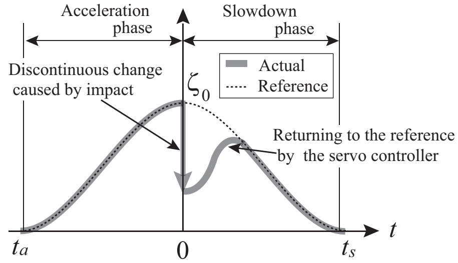

Fig. 3. Reference and actual behavior of interpolated trajectories.

constraint. From (7), the minimum norm solution of the joint angle velocity can be obtained as follows:

$$\dot{\boldsymbol{\phi}} = \begin{bmatrix} \boldsymbol{J}_{hu} \\ \boldsymbol{C}_{\alpha} \end{bmatrix}^{\dagger} \begin{bmatrix} \boldsymbol{V} \\ \mathbf{0} \end{bmatrix} \equiv \boldsymbol{A}^{\dagger} \begin{bmatrix} \boldsymbol{V} \\ \mathbf{0} \end{bmatrix}, \tag{9}$$

where $\boldsymbol{A}^{\dagger}$ indicates pseudoinverse matrix [9] of $\boldsymbol{A}$. In order to consider the angle movable range of all joints, the pesudoinverse matrix in (9) can be modified as follows:

$$\boldsymbol{A}_w^{\dagger} = \boldsymbol{W}^{-1}\boldsymbol{A}^T \left(\boldsymbol{A}\boldsymbol{W}^{-1}\boldsymbol{A}^T\right), \tag{10}$$

where $\boldsymbol{W}$ is a matrix of weights [10]. The elements of the matrix can be denotes as follows:

$$w_i^k = \begin{cases} \frac{1}{\phi_{i,um}^k} & \phi_{i,um}^k \le \phi_{i,lm}^k \\ \frac{1}{\phi_{i,lm}^k} & \phi_{i,um}^k > \phi_{i,lm}^k \\ \infty & \phi_{i,um}^k < 0 \quad \text{or} \quad \phi_{i,lm}^k < 0 \end{cases},$$

where w_i^k is a diagonal element corresponding to $\dot{\phi}_i^k$ ($k = rl,\ ll,\ ch,\ ra$ or rl) and subscript i and superscript k denotes the joint number and the arm number, respectively. And $\phi_{i,um}^k$ and $\phi_{i,lm}^k$ are computed using upper joint angle limit of ith-joint $\phi_{i,ulim}^k$ and lower limit $\phi_{i,llim}^k$ as follows:

$$\phi_{i,um}^k \equiv \phi_{i,ulim}^k - \phi_i^k, \quad \phi_{i,lm}^k \equiv \phi_i^k - \phi_{i,llim}^k, \tag{11}$$

Therefore, the solution can be obtained as follows:

$$\dot{\boldsymbol{\phi}} = \boldsymbol{A}_w^{\dagger} \begin{bmatrix} \boldsymbol{V} \\ \mathbf{0} \end{bmatrix}. \tag{12}$$

C. Generating Acceleration and Slowdown Motions

After deciding the velocity of the end effector, the momentum, the angular momentum and the velocity of CoM, these values are interpolated from zero and to zero. In order to avoid discontinuous of first order derivatives of these values, the trajectories are interpolated by third-order polynomial [9] as shown in Fig. 3. The dotted line expresses interpolated trajectory. By using the interpolated trajectories, the joint velocities are computed by (12). The motion is generated from $t = 0$ to $t = t_s$. This motion generating method is based on combinatorial control of resolved momentum control [11] and COG Jacobian [12]. In this study, interpolation time t_s is decided empirically. However, the parameter should be decided considering performance of the actuators. This parameter will be considered as a decision variable in the future study.

The acceleration and slowdown motions are generated based on a result of optimization problem described in the next subsection. The assumed actual behavior of the interpolated trajectories is shown in Fig. 3. The discontinuous change is occurred at the time of impact by impulsive force. However, the actual trajectory returns to the reference one immediately by the servo controller.

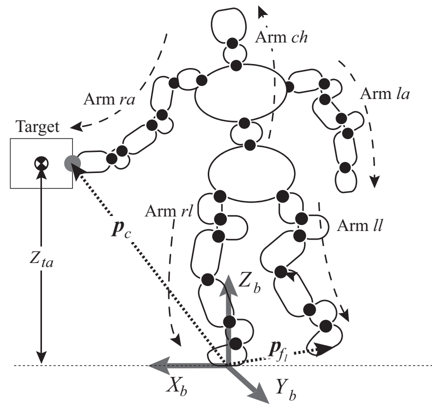

Fig. 4. Notations of a HRP-2 model.

D. Formulation of the Optimization Problem

By using the simplified contact dynamics computation model [6], peak force or impulse exerted on a target object can be obtained. Therefore, the object of this optimization problem is to maximize the peak force or impulse by varying robot's posture and angle velocities. As stated in Subsection III-A and III-B , the posture and angle velocities can be obtained by giving the following values.

- The position vector of the right foot with respect to Σ_0.
- The right foot's Z-Y-X Euler angle with respect to Σ_0.
- The position vector of the left foot with respect to the right foot coordinate system.
- The joint angles except for the leg joints.
- The collision velocity v_c in X_b direction.
- The momentum in Z_b direction, the angular momentum around X_b and Y_b axes.
- The velocity of the center of mass.

Therefore, the decision variables are expressed as follows:

$$\boldsymbol{x} = \begin{bmatrix} {}^0\boldsymbol{p}_{f_r}{}^T & {}^0\boldsymbol{\alpha}_{f_r}{}^T & {}^{f_r}\boldsymbol{s}_{f_l}{}^T & \boldsymbol{\phi}^{remT} & v_c & \boldsymbol{\mathcal{M}}^T & \boldsymbol{v}_{Tg_{xy}}{}^T \end{bmatrix}, \tag{13}$$

and the ranges of the variables are denoted as follows:

$$\begin{aligned} {}^{min,0}p_{\eta,f_r} \le {}^0p_{\eta,f_r} \le {}^{max,0}p_{\eta,f_r} \quad & (\eta = x, y, z), \\ {}^{min,0}\alpha_{\eta,f_r} \le {}^0\alpha_{\eta,f_r} \le {}^{max,0}\alpha_{\eta,f_r} \quad & (\eta = x, y, z), \\ {}^{min,f_r}s_{\eta,f_l} \le {}^{f_r}s_{\eta,f_l} \le {}^{max,f_r}s_{\eta,f_l} \quad & (\eta = x, y, z), \\ {}^{min}\phi_i^{rem} \le \phi_i^{rem} \le {}^{max}\phi_i^{rem}, & \\ {}^{min}v_c \le v_c \le {}^{max}v_c, & \\ {}^{min}P_z \le P_z \le {}^{max}P_z, & \\ {}^{min}L_\eta \le L_\eta \le {}^{max}L_\eta \quad & (\eta = x, y), \\ {}^{min}v_{g\eta} \le v_{g\eta} \le {}^{max}v_{g\eta} \quad & (\eta = x, y), \end{aligned}$$

where ${}^{min,0}p_{x,f_r}$ and ${}^{min,0}p_{x,f_r}$ indicate respectively the minimum value and maximum value of ${}^0p_{x,f_r}$ and the others are defined similarly. The position of the target box relative to the robot is illustrated in Fig. 4.

The objective function for impact motions is obviously the peak force f_{max} or impulse $\bar{f}_n$. The objective value is decided based on a task whether the force or impulse. This optimization problem is expressed as follows and this optimizing problem can be solved by SQP (Sequential Quadratic Programming).

$$
\begin{aligned}
&\text{minimize} \quad f(\boldsymbol{x}) = -f_{max} \quad \text{or} \quad -\bar{f}_n, \\
&\text{subject to}
\end{aligned}
$$

$$
\left\{
\begin{array}{l}
\left.\begin{array}{ll}
(z_{ta} - z_{te}) \leq \boldsymbol{n}_z^T \boldsymbol{p}_c \leq (z_{ta} + z_{te}), & \\
{}^{min}R_{ce} \leq \boldsymbol{n}_x^T \boldsymbol{R}_c \boldsymbol{n}_h \leq {}^{max}R_{ce}, & \\
-v_{\eta,ce} \leq v_{\eta,c} \leq v_{\eta,ce}, & (\eta = y, z) \\
-\omega_{\eta,ce} \leq \omega_{\eta,c} \leq \omega_{\eta,ce}, & (\eta = x, y, z)
\end{array}\right\} \boxed{1} \\
\left.\begin{array}{l}
-z_{fe} \leq \boldsymbol{n}_z^T \boldsymbol{p}_{f_l} \leq z_{fe}, \\
{}^{min}R_{fe} \leq \boldsymbol{n}_x^T \boldsymbol{R}_{f_l} \boldsymbol{n}_z \leq {}^{max}R_{fe}, \\
\|\dot{\boldsymbol{p}}_{f_l}\| \leq v_{fe}, \\
\|\boldsymbol{\omega}_{f_l}\| \leq \omega_{fe},
\end{array}\right\} \boxed{2} \\
\left. l_{Z_{imp}} \geq l_{Z_{imp}e}, \right\} \boxed{3} \\
\left. l_{Z_{as}} \geq l_{Z_{as}e}, \right\} \boxed{4} \\
\left.\begin{array}{l}
\left(\phi^k_{i,llim} + C_\phi\right) \leq \phi^k_i \leq \left(\phi^k_{i,ulim} - C_\phi\right), \quad (k = rl, ll) \\
-C_v \dot{\phi}^k_{i,lim} \leq \dot{\phi}_i^{\,k} \leq C_v \dot{\phi}^k_{i,lim},
\end{array}\right\} \boxed{5} \\
\left.\begin{array}{l}
{}^{min}P_\eta \leq P_\eta \leq {}^{max}P_\eta, \quad (\eta = x, y) \\
{}^{min}L_z \leq L_z \leq {}^{max}L_z,
\end{array}\right\} \boxed{6}
\end{array}
\right.
\tag{14}
$$

where

$\boldsymbol{p}_c \in R^{3\times1}$	: position vector of the contact point (Fig. 4),
$\boldsymbol{R}_c \in R^{3\times3}$	: rotation matrix of the end effector,
z_{ta}	: hight of the target point,
z_{te}	: allowed error in the hight,
$\boldsymbol{n}_z \in R^{3\times1}$	: unit vector pointing Z_b direction,
$\boldsymbol{n}_x \in R^{3\times1}$	: unit vector pointing X_b direction,
${}^c\boldsymbol{n}_h \in R^{3\times1}$	: unit vector pointing the collision direction with respect to the local coordinate of the end effector,
${}^{min}R_{ce}, {}^{max}R_{ce}$	: allowed rage of the collision direction,
$v_{\eta,c}$	: velocity of the contact point in η direction,
$\omega_{\eta,c}$	: angular velocity of the contact point around η axis,
$v_{\eta,ce}$	: allowed velocity of the contact point in η direction,
$\omega_{\eta,ce}$	: allowed angular velocity of the contact point around η axis,
z_{fe}	: allowed error in the foot from the ground,
$\boldsymbol{p}_{f_l} \in R^{3\times1}$	: position vector of the left foot,
$\boldsymbol{R}_{f_l} \in R^{3\times3}$	: rotation matrix of the left foot,
${}^{min}R_{fe}{}^{max}R_{fe}$	: allowed rage of the left foot's orientation,
$\boldsymbol{\omega}_{f_l} \in R^{3\times1}$	: angular velocity of the left foot,
v_{fe}	: allowed norm of the left foot's velocity,
ω_{fe}	: allowed norm of the left foot's angular velocity,
$l_{Z_{imp}}$	: minimum distance of ZMP from a support polygon during impact phase,
$l_{Z_{imp}e}$	: margin for $l_{Z_{imp}}$,
$l_{Z_{as}}$	: minimum distance of ZMP from a support polygon during acceleration/slowdown phases,
$l_{Z_{as}e}$	: margin for $l_{Z_{as}}$,
$\phi^k_{i,llim}$	: lower joint angle limit of i-th joint of arm k,
$\phi^k_{i,ulim}$	: upper joint angle limit of i-th joint of arm k,
C_ϕ	: margin for the leg joint angle limit,
$\dot{\phi}^k_{i,lim}$	: joint angle velocity limit of i-th joint of arm k,
C_v	: margin for the leg joint angle velocity limit,
P_η	: momentum in η direction,
${}^{min}P_\eta, {}^{max}P_\eta$	: allowed range of momentum in η direction,
L_z	: angular momentum around Z_b axis,
${}^{min}L_z, {}^{max}L_z$	: allowed range of angular momentum around Z_b.

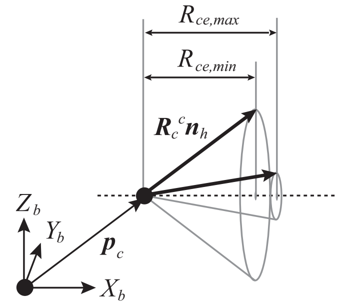

Fig. 5. Allowed range of the colliding direction.

In (14), the kinematics and ZMP are computed on the assumption that the right foot is fixed on the ground. The part $\boxed{1}$ expresses constraints depended on the task. In this case (Fig. 2), this part defines behavior of the hand and the box at the time of impact. Fig. 5 explains allowed range of the colliding direction. In the figure, ${}^c\boldsymbol{n}_h$ is an unit vector pointing the collision direction in the local coordinate of the end effector. In this case, since the robot punches the box to negative direction in Z direction with respect to the local coordinate of the end effector, ${}^c\boldsymbol{n}_h$ is $\begin{bmatrix} 0 & 0 & -1 \end{bmatrix}^T$. The part $\boxed{2}$ expresses constraints for the both legs and avoids generating internal forces. Though the kinematic closure is defined by (8), the solution (12) using pesudoinverse does not guarantee the constraints. Therefore, the constraint is defined here. The parts $\boxed{3}$ and $\boxed{4}$ express stability during impact phase and acceleration/slowdown phases, respectively. These parts keep ZMP inside of a support polygon. $l_{Z_{imp}}$ is computed by SDC model and $l_{Z_{as}}$ is computed by the ZMP estimation scheme for acceleration/slowdown phases stated in Section II CoM, angular momentum and momentum at the time of impact are interpolated by third-order polynomial as shown in Fig.3. By using the interpolated trajectories, ZMP during acceleration/slowdown phases are computed by (1) without computing the inverse dynamics and distance between support polygon and ZMP is evaluated. Therefore, the part $\boxed{4}$ guarantees the stability during acceleration/slowdown phases in the optimization process.

The part $\boxed{5}$ defines hardware limitation of the robot' legs. The part $\boxed{6}$ expresses limitation of momentums in X_b and Y_b directions and angular momentum around Z_b axis. These are related to friction between a floor and the feet.

IV. SIMULATION RESULT

In order to evaluate the proposed scheme, a punching motion is generated to perform by the humanoid robot HRP-

TABLE I

DECISION VARIABLES ${}^{0}\boldsymbol{p}_{f_r}$, ${}^{0}\boldsymbol{\alpha}_{f_r}$, ${}^{f_r}\boldsymbol{s}_{f_l}$, v_c, $\boldsymbol{\mathcal{M}}$ AND $\boldsymbol{v}_{Tg_{xy}}$

init.	min.	max.	result	init.	min.	max.	result
${}^{0}p_{x,f_r}$ (m)				${}^{0}p_{y,f_r}$ (m)			
0.00	−0.15	0.15	−0.15	−0.095	−0.25	−0.095	−0.14
${}^{0}p_{z,f_r}$ (m)				${}^{0}\alpha_{x,f_r}$ (°)			
−0.30	−0.60	−0.30	−0.60	0.00	−0.01	0.01	0.01
${}^{0}\alpha_{y,f_r}$ (°)				${}^{0}\alpha_{z,f_r}$ (°)			
0.00	−10.00	10.00	−8.73	0.00	−0.01	0.01	0.01
${}^{f_r}s_{x,f_l}$ (m)				${}^{f_r}s_{y,f_l}$ (m)			
0.00	−0.30	0.30	0.30	0.19	0.19	0.45	0.19
v_c (m/s)				P_z (Ns)			
2.00	∞	0.00	2.4	0.00	−3.00	3.00	2.68
L_x (Nms)				L_y (Nms)			
0.00	−3.00	3.00	3.00	0.00	−3.00	3.00	3.00
v_{gx} (m/s)				v_{gy} (m/s)			
0.00	$-\infty$	∞	0.09	0.00	$-\infty$	∞	−0.06

TABLE II

DECISION VARIABLE $\boldsymbol{\phi}^{rem}$

	ϕ_1^{ch}	ϕ_2^{ch}	ϕ_1^{ra}	ϕ_2^{ra}
init. (°)	−21.5	17.1	3.2	−17.9
min. (°)	−25.0	15.0	−160.0	−75.0
max. (°)	25.0	40.0	40.0	−10.0
result (°)	−22.4	15.0	−12.4	−10.0
	ϕ_3^{ra}	ϕ_4^{ra}	ϕ_5^{ra}	ϕ_6^{ra}
init. (°)	−14.1	−74.4	26.2	−46.8
min. (°)	−72.0	−97.0	−52.0	−52.0
max. (°)	72.0	−38.0	52.0	52.0
result (°)	−8.6	−56.1	30.8	−52.0

TABLE III

THE JOINT ANGLES OF THE NECK, RIGHT ARM AND HANDS.

Joint	ϕ_3^{ch}	ϕ_4^{ch}	ϕ_7^{ra}	ϕ_1^{la}	ϕ_2^{la}
(°)	0.0	0.0	0.0	18.4	45.0
Joint	ϕ_3^{la}	ϕ_4^{la}	ϕ_5^{la}	ϕ_6^{la}	ϕ_7^{la}
(°)	1.2	−27.5	0.0	−10.0	0.0

2 [13]. A HRP-2 model of this simulation is modified from an original HRP-2 model. The arrangement of wrist axes is modified original HRP-2 [14]. Fig. 4 illustrates the HRP-2 model and its notations. The objective function is chosen as follows as an example.

$$f(\boldsymbol{x}) = -f_{max}. \tag{15}$$

In order to simplify the problem, the joint angles of the left arm, neck and hand are not included in decision variables. Tables I and II show the initial, minimum and maximum values of the decision variables. ϕ_i^{ch} expresses the chest and neck joint angles. The range of these decision variables are decided based on hardware limitation of HRP-2 and the initial values are chosen heuristically. If P_x, L_x and L_y are huge, the robot cannot accelerate the body during acceleration phase. Therefore, P_x, L_x and L_y are limited. The ranges of these momentums are decided in moderation. It is a future work to decide these limits theoretically considering the robot's actuator performance. Table III shows the joint angles which are not included in the decision variables. $\phi_{3\sim4}^{ch}$, ϕ_7^{ra} and ϕ_i^{la} are neck joint angles, right hand joint angle and left arm joint angles including its hand, respectively. The angles are decided intuitively to avoid collision between the left arm and the body.

The constraint conditions are shown in Table IV. The height and mass of the target box are 0.7 (m) and 5 (kg), respectively. Therefore, z_{ta} is 0.7 (m). The other constraint conditions are examples of the conditions for the punching motion.

This optimization problem is solved by using the technical computing language MATLAB (The MathWorks, Inc.) and Optimization Toolbox. The motion is generated in 633 (s) by two 3 (GHz) Intel Xeon X5365 CPUs.

Fig. 6 shows transition from the initial posture to an optimal posture. The initial posture does not satisfy the constraint conditions. For example, the height of the hand is lower than the required position. The optimal posture satisfy all the constraint conditions. As shown in Fig. 6 (b), the robot's torso shifts forward. ZMP moves backward when the robot receives impulsive force. In order to extend the margin of the support polygon backward, the robot's center of mass shifts forward. Table I and II show the optimized result of the decision variables. The hand collides with the box at 2.4 (m/s). In order to extend the support polygon in front-back direction, ${}^{f_r}s_{x,f_l}$ reaches its maximum limit 0.3 (m). To hit the box strongly, L_x and L_y reach their maximum limit.

In order to generate motions for acceleration and slow-down phases, interpolation time t_a and t_s of v_c are $-0.7/4$ (s) and $0.7/4$ (s), respectively. And t_a and t_s of P_x, L_x, L_y, v_{gx} and v_{gy} are 0.7 (s) and -0.7 (s), respectively. In Fig. 7, the dotted lines show the momentum and angular momentum of the generated motion. The momentums and angular momentum are obtained by inverse dynamics on the assumption that the right foot is fixed on the ground from the generated motion. The computational results of P_z, L_x and L_y at the time of impact are respectively 2.7 (Ns), 3.0 (Nms) and 3.0 (Nms) as shown in Table I. In Fig. 7, the dotted lines show that P_z, L_x and L_y are smoothly interpolated from zero and to zero during the acceleration and slowdown phases.

Fig. 8 shows snapshots of the OpenHRP3 [15] simulation result. The simulation condition, e.g. contact model between the hand and the box, is the same with [6]. As shown int these figures, the robot dexterously accelerates and slows down the body by twisting its torso. Since the momentum in Z_b direction is positive at time of impact, the robot unbends the body after the impact as shown in Fig. 8 . Fig. 9 shows the estimated impulsive force in the optimizing process and OpenHRP3 simulation result. The estimated and actual peak force are 734.9 (N) and 722.0 (N) respectively and the error is -1.8 (%). The estimated and actual impulses are 15.1 (Ns) and 13.4 (Ns) respectively and the error is -12.6 (%). Fig. 10 shows the ZMP trajectory during the three phases. ZMP shifts backward during impact phase. Then, ZMP shifts forward during slowdown phase. The distance from the edge of the support polygon is minor during the both phase. This

TABLE IV

CONSTRAINT CONDITIONS.

z_{ta} (m)	$z_{te}(m)$	${}^{min}R_{ce}$	${}^{min}R_{ce}$
0.7	0.01	0.9962	1.0
$v_{y,ce}$ (m/s)	$v_{z,ce}$ (m/s)	$\omega_{x,ce}$ (°/s)	$\omega_{y,ce}$ $(°/s)$
0.3	0.3	5.0	5.0
$\omega_{z,ce}$ $(°/s)$	z_{fe}	${}^{min}R_{fe}$	${}^{max}R_{fe}$
5.0	0.003	0.9962	1.0
v_{fe} (m/s)	ω_{fe} (°/s)	$l_{Z_{impe}}$ (m)	$l_{Z_{ase}}$ (m)
0.01	0.01	0.05	0.05
C_ϕ (°)	C_v	${}^{min}P_x$ (Ns)	${}^{max}P_x$ (Nms)
5.0	0.8	-5.0	5.0
${}^{min}P_y$ (Ns)	${}^{max}P_z$ (Ns)	${}^{min}L_z$ (Nms)	${}^{max}L_z$ (Nms)
-5.0	-5.0	5.0	5.0

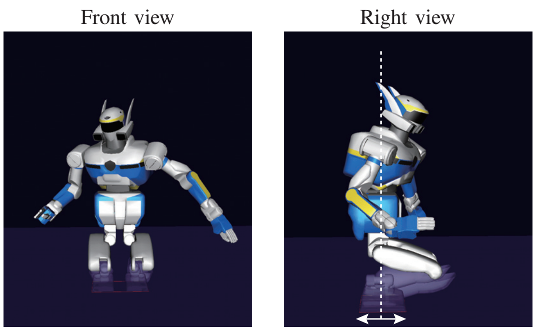

(a) Initial posture

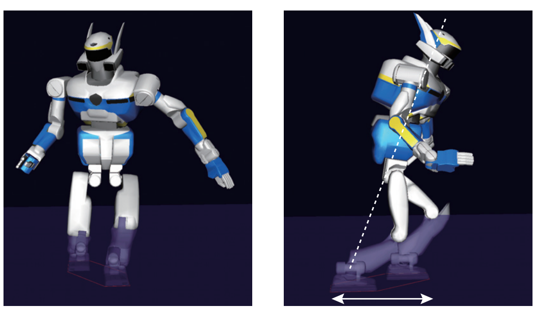

(b) Optimal posture

Fig. 6. Comparison between the initial posture and optimal posture.

result indicate this motion uses the support polygon fully.

In order to see the trajectory in time domain, Fig. 11 shows the relationship between ZMP and time. In the figure, the blue line and red line indicate the predicted ZMP trajectory and OpenHRP3 result, respectively. The blue line computed by inverse dynamics from the reference motion. Therefore, the behavior of ZMP during the impact phase does not consider. The dotted lines indicate the impact phase. Except for the impact phase, the trend of the estimated ZMP trajectories during the acceleration and slowdown phase is similar to the OpenHRP3 simulation. The behavior of ZMP during the impact phase is predicted by the proposed SDC model. Fig. 11 shows the detail during the impact phase. The blue line is computed by SDC. The dotted line indicates the end of the impact phase. The trend of the estimated ZMP trajectories during the impact phase is similar to the OpenHRP3 simulation. Therefore, this scheme predicts ZMP trajectories accurately for all phases and optimizes the

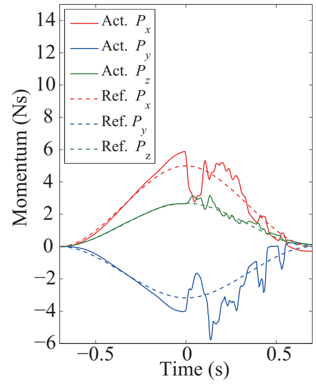

(a) Momentum

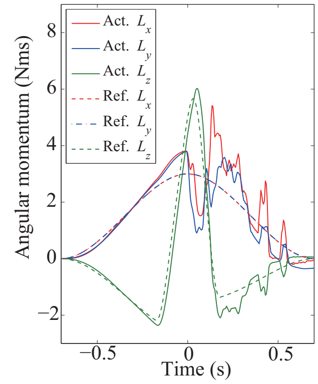

(b) Angular momentum

Fig. 7. Reference and actual momentum and angular momentum in Σ_b.

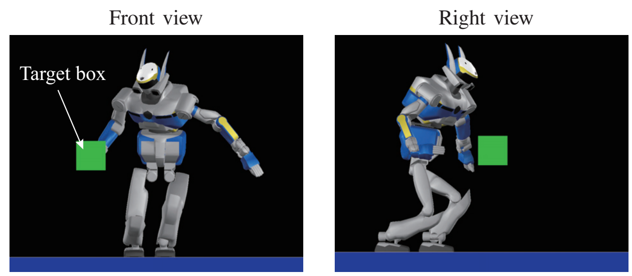

(a) -0.6 (s)

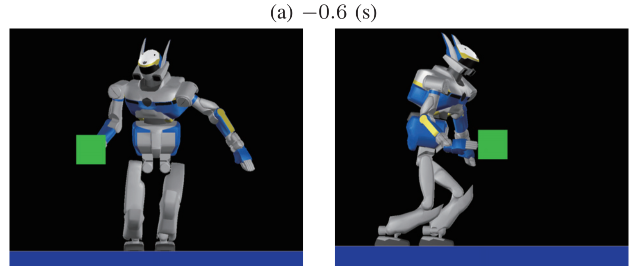

(b) 0.0 (s)

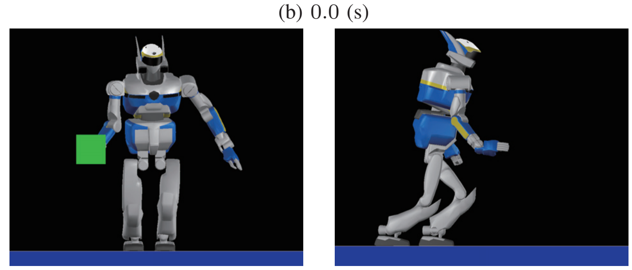

(b) 0.6 (s)

Fig. 8. Simulation of the optimized motion.

motion.

Fig. 7 shows the momentum and angular momentum in Σ_b coordinate system. The solid lines indicate the momentums and angular momentum simulated by OpenHRP3. The actual momentum and angular momentum follow the reference during the early acceleration phase. From -0.2 (s) to 0 (s), P_x, P_y, L_x and L_y overshoot the reference. At 0 (s), the drastic changes are occurred. Then, the servo controller tries to follow the reference during the slowdown phase. The behavior is similar to the assumption expressed in Fig. 3.

V. CONCLUSIONS

In order to maximize the impulsive force exerted on a target, the impact motion is generated through optimization

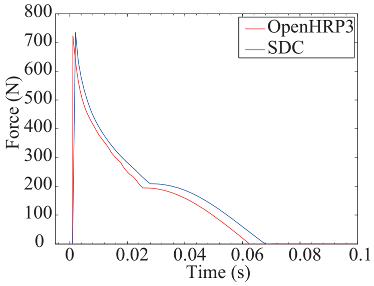

Fig. 9. Estimated impulsive force and OpenHRP3 simulation result.

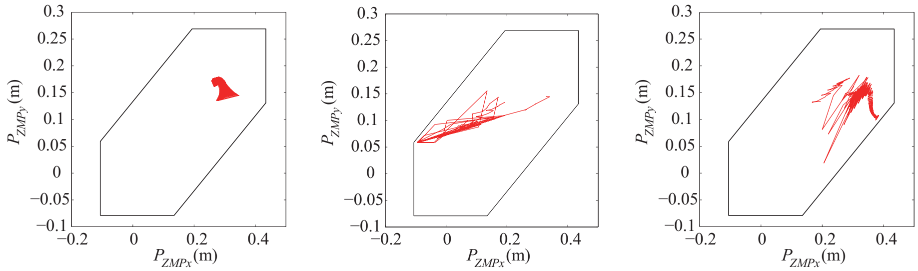

(a) Acceleration phase (b) Impact phase (c) Slowdown phase

Fig. 10. ZMP trajectory measured by OpenHRP3.

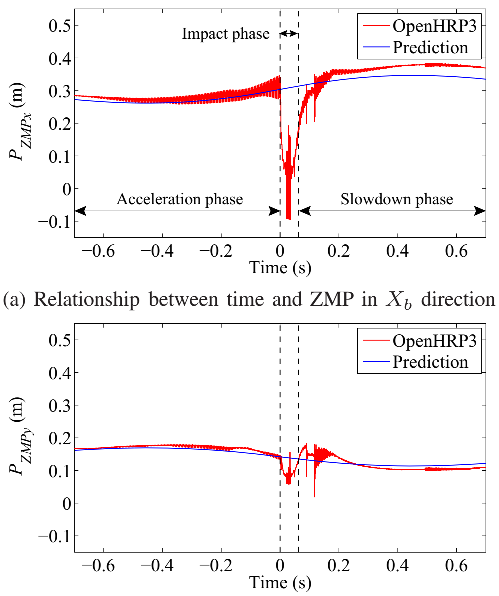

(a) Relationship between time and ZMP in X_b direction

(b) Relationship between time and ZMP in Y_b direction

Fig. 11. Predicted ZMP trajectory and OpenHRP3 simulation result.

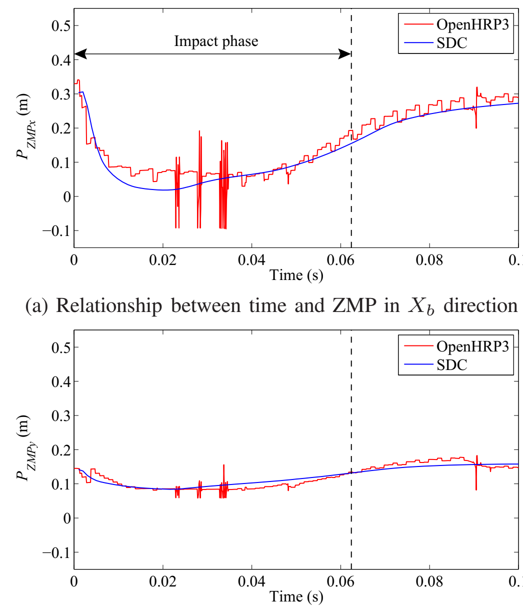

(a) Relationship between time and ZMP in X_b direction

(b) Relationship between time and ZMP in Y_b direction

Fig. 12. Detail of the ZMP trajectory during the impact phase.

method considering postural stability during acceleration, impact and slowdown phases. With this scheme, the stability during the acceleration and slowdown phase can be evaluated in the optimizing process without computing inverse dynamics. The impact motion generated by this scheme is evaluated by performing simulationsk. The estimated force and ZMP trajectories are similar to OpenHRP3 simulation result. This scheme will be evaluated by a real humanoid robot in a future study.

References

[1] M. Uchiyama, "A control algorithm constitution method for aritificial arm and dynamic control modes," in *Biomechanism 3*. University of Tokyo Press, 1975, (in Japanese).

[2] H. Asada and K. Ogawa, "On the dynamic analysis of a manipulator and its end effector interacting with the environment," in *Proc. of the 1987 IEEE Int. Conf. on Robotics and Automation*, vol. 2, pp. 751–756, 1987.

[3] O. Khatib and J. Burdick, "Motion and force control of robot manipulators," in *Proc. of the 1986 IEEE Int. Conf. on Robotics and Automation*, pp. 1381–1386, 1986.

[4] A. Konno *et al.*, "Optimization of impact motions for humanoid robots," in *Proc. of the 2008 IEEE/RSJ Int. Conf. on Intelligent Robots and Systems*, pp. 647–652, 2008.

[5] H. Arisumi and K. Yokoi, "Whole-body motion of a humanoid robot for passing through a door," in *Proc. of the 9th SICE System Integration Division Annual Conf.*, pp. 1067–1068, 2008, (in Japanese).

[6] T. Tsujita, A. Konno, and M. Uchiyama, "Contact dynamics modeling of a humanoid robot for tasks utilizing impact dynamics," in *Proc. of the 2009 IEEE/RSJ Int. Conf. on Intelligent Robots and Systems*, pp. 447–452, 2009.

[7] M. Vukobratović *et al.*, *Biped Locomotion – Dynamics, Stability, Control and Application*. Springer-Verlag, 1990.

[8] K. Yoshida, R. Kurazume, and Y. Umetani, "Dual arm coordinate in space free-flying robot," in *Proc. of the 1991 IEEE Int. Conf. on Robotics and Automation*, vol. 3, pp. 2516–2521, 1991.

[9] T. Yoshikawa, *Foundations of Robotics*. MIT Press, 1990.

[10] J. Hollerbach and K. Suh, "Redundancy resolution of manipulators through torque optimization," *IEEE J. of Robotics and Automation*, vol. 3, no. 4, pp. 308–316, 1987.

[11] S. Kajita *et al.*, "Resolved momentum control: humanoid motion planning based on the linear and angular momentum," in *Proc. of the 2003 IEEE/RSJ Int. Conf. on Intelligent Robots and Systems*, pp. 1644–1650, 2003.

[12] T. Sugihara and Y. Nakamura, "Whole-body cooperative balancing of humanoid robot using COG jacobian," in *Proc. of the 2002 IEEE Int. Conf. on Intelligent Robots and Systems*, pp. 2575–2580, 2002.

[13] K. Kaneko *et al.*, "Humanoid robot HRP-2," in *Proc. of the 2004 IEEE Int. Conf. on Robotics and Automation*, pp. 1083–1090, 2004.

[14] T. Tsujita *et al.*, "Humanoid robot motion generation for nailing task," in *Proc. of the 2008 IEEE/ASME Int. Conf. on Advanced Intelligent Mechatronics*, pp. 1024–1029, 2008.

[15] S. Nakaoka *et al.*, "Constraint-based dynamics simulator for humanoid robots with shock absorbing mechanisms," in *Proc. of the 2007 IEEE/RSJ Int. Conf. on Intelligent Robots and Systems*, pp. 3641–3647, 2007.